PNAS RESEARCH ARTICLE | EARTH, ATMOSPHERIC, AND PLANETARY SCIENCES

Oceanic intraplate explosive eruptions fed directly from the mantle

Charlotte L. DeVitre[a,1], Esteban Gazel[a,1], Ricardo S. Ramalho[b,c,d], Swetha Venugopal[e,f], Matthew Steele-MacInnis[g], Junlin Hua[h], Chelsea M. Allison[i], Lowell R. Moore[j], Juan Carlos Carracedo[k], and Brian Monteleone[l]

Edited by Roberta Rudnick, University of California, Santa Barbara, CA; received February 6, 2023; accepted June 22, 2023

Constraining the volatile content of magmas is critical to our understanding of eruptive processes and their deep Earth cycling essential to planetary habitability [R. Dasgupta, M. M. Hirschmann, *Earth Planet. Sci. Lett.* 298, 1 (2010)]. Yet, much of the work thus far on magmatic volatiles has been dedicated to understanding their cycling through subduction zones. Further, studies of intraplate mafic volcanism have disproportionately focused on Hawaii [P. E. Wieser et al., *Geochem. Geophys. Geosyst.* 22, e2020GC009364 (2021)], making assessments of the overall role of intraplate volcanoes in the global volatile cycles a challenge. Additionally, while mafic volcanoes are the most common landform on Earth and the Solar System [C. A. Wood, *J. Volcanol. Geotherm. Res.* 7, 387–413 (1980)], they tend to be overlooked in favor of silicic volcanoes when it comes to their potential for explosivity. Here, we report primitive (olivine-hosted, with host Magnesium number – Mg# 78 to 88%) melt inclusion (MI) data from Fogo volcano, Cabo Verde, that suggest that oceanic intraplate silica-undersaturated explosive eruptions sample volatile-rich sources. Primitive MI (melt Mg# 70 to 71%) data suggest that these melts are oxidized (NiNiO to NiNiO+1) and very high in volatiles (up to 2 wt% CO_2, 2.8 wt% H_2O, 6,000 ppm S, 1,900 ppm F, and 1,100 ppm Cl) making Fogo a global endmember. Storage depths calculated from these high volatile contents also imply that magma storage at Fogo occurs at mantle depths (~20 to 30 km) and that these eruptions are fed from the mantle. Our results suggest that oceanic intraplate mafic eruptions are sustained from the mantle by high volatile concentrations inherited from their source and that deep CO_2 exsolution (here up to ~800 MPa) drives their ascent and explosivity.

intraplate volcanoes | volatiles | mantle | melt inclusions | Fogo

Significance

The role of intraplate volcanoes in the global volatile cycle and their potential to produce explosive eruptions are still major unknowns. Using melt inclusions (MIs) from mafic explosive eruptions from Fogo, one of the world's most active volcanoes with highly explosive mafic eruptions, we can start answering those questions. We identified that Fogo sampled a volatile-rich mantle source and represents an important global endmember, as evidenced by MIs that record oxidized melt compositions and very high volatile concentrations (2 wt% CO_2, 2.8 wt% H_2O, 6,000 ppm S, 1,900 ppm F, and 1,100 ppm Cl). Our observations imply that eruptions such as these are fed directly from the mantle, bypassing shallow crustal storage, and are driven up by deep CO_2 exsolution.

Studies of volatiles (H_2O, CO_2, S, Cl, and F) in magmatic systems are critical to elucidate volcanic processes from source to surface. Volatiles influence melting and formation of ore deposits, their degassing impacts volcanic explosivity, and volatile cycling through the Earth plays an essential role in sustaining planetary habitability (1–3). Much of the work on volatiles in magmatic systems over the past decades has focused on subduction zones and mid-ocean ridges (MOR) which collectively output over 90% of the annual magma production on Earth (4). MORs output ~75% of the magmas on Earth every year, but their volatile contents are typically very low [<0.3 wt% (3)] relative to intraplate volcanoes, which produce <10% of the yearly magmatic output and contain >5 wt% volatiles (5). Despite this, very little volatile data are available on intraplate volcanoes (except for Hawaii), and our understanding of their contribution to the global volatile cycles remains thus limited. Intraplate volcanoes offer the best information on the chemistry and volatile content of a diversity of Earth's mantle sources and thus are key to build a complete scenario of our planet's deep internal dynamics and composition.

Studies of volatile species are challenging given their low solubility in magmas at low pressures. Indeed, most magmas are almost entirely degassed by the time they reach the surface (3) and estimates of volatiles made on lavas, or the glass fraction of tephra (especially when erupted subaerially) can severely underestimate the pre-eruptive volatile contents of magmas. Fortunately, melt inclusions (MIs), tiny droplets of melt trapped during crystal growth, can retain much of the original volatile contents of the magma at the time of entrapment (though complexities exist) and are therefore the best tool to inform studies seeking to understand the pre-eruptive volatile contents of magmas, volatile evolution during eruption, and magma degassing and decompression pathways (6–10).

Determining the factors that control volcanic explosivity is a challenging task, as they are driven by complex processes at interplay with each other, from magmatic drivers, such as composition, pre-eruptive volatile content, volatile solubility and exsolution, viscosity, and temperature (11–13) to crustal properties like tectonic regime, stress fields, and conduit and vent geometry (12–14). Magma properties evolve during storage and ascent, and as magma cools and undergoes fractional crystallization, assimilation, and mixing, viscosity and volatile

The authors declare no competing interest.

This article is a PNAS Direct Submission.

[1]To whom correspondence may be addressed. Email: cld243@cornell.edu or egazel@cornell.edu.

This article contains supporting information online at https://www.pnas.org/lookup/suppl/doi:10.1073/pnas.2302093120/-/DCSupplemental.

Published August 7, 2023.

contents increase leading to a rising potential for explosivity (13, 15–17). Because of this, it is difficult to discern the relative importance of each process, especially when comparing volcanoes that differ significantly in composition or tectonic setting.

Although it is assumed that H_2O is the main volatile that drives ascent and explosivity (18), it is not always the case that the most explosive mafic eruptions are those with the highest pre-eruptive H_2O contents (10, 19–21). Recent work has proposed a role for CO_2 in driving the ascent of explosive basaltic eruptions at continental intraplate volcanoes (10), and there is statistical evidence that mantle sources with higher volatile contents may contribute to more explosive eruptive styles (22). This motivates the question of whether it is truly H_2O diffusion and exsolution that initially drive the decompression rate of mafic magmas or whether CO_2, which exsolves at a greater depth, plays a crucial and definite role in determining the explosivity of mafic volcanism. And if the latter, are unusually high CO_2 contents inherited from the mantle source or a result of the melting style alone? The answer to this question is simultaneously critical to our scientific understanding of eruptive initiation and evolution and to the forecast of the unexpectedly explosive extrusion of mafic magmas at oceanic intraplate volcanoes.

1. Fogo Volcano, Cabo Verde

Fogo, an oceanic intraplate volcano in the Cabo Verde Archipelago (CVA, Fig. 1), is one of the world's most active ocean island volcanoes with ~30 mafic eruptions since historic records started in the 15th century [most recent cycles occurred in 1951, 1995, and 2014 to 2015 (23)]. It erupts predominantly basanitic magma (24), which is characterized by incredibly low viscosities (25) simplifying the scenario that allows to understand the role of volatiles in explosivity. Additionally, Fogo hosted highly explosive eruptions (sub-Plinian, Plinian to ultra-Plinian), occurring every ~3 ky, the vast majority (~90%) of which are mafic in composition (26). Fogo is therefore the ideal testbed to investigate how the volatile composition controls the explosivity of mafic magmas sourced directly from the mantle.

The CVA also represents an interesting oceanic intraplate endmember (39) given the nature of its silica-undersaturated (nepheline normative) lavas that are indicative of very high CO_2 contents (Fig. 1*A*, calculation based on ref. 27). Silica-undersaturated compositions from other locations are thought to sample a volatile-rich source, perhaps stored in the mantle transition zone (40, 41). Global tomography suggests that there is a deeply rooted plume below the CVA (42), although this signal is not as strong in the upper mantle as it is below the transition zone, opening the possibility that the transition zone may also be upwelling due to instabilities caused by the plume, or that the plume itself interacts with the transition zone. Likewise, it has been inferred from the ubiquitous presence of extrusive and intrusive carbonatites in the volcanic sequences of the CVA (39), that the CVA samples a CO_2-rich source. Finally, Fogo's daily fumarolic CO_2 output (~1,060 t/day) rivals the emissions of the highest actively degassing volcanoes on Earth (43). Despite all this, there is extremely limited literature data available on magmatic volatiles for Fogo and the CVA, and future high-intensity events would pose a significant threat to the Cape Verdean population and trans-Atlantic air traffic. For all these reasons, Fogo is a critical location to study the origin of high CO_2 contents in silica-undersaturated oceanic intraplate magmas and the role of CO_2 in driving mafic explosivity. Here, we present a comprehensive MI study of three mafic explosive eruptions Fogo (*SI Appendix*, section 1), aiming to shed light on the pre-eruptive volatile composition at this volcano, to assess depths of entrapment and storage, and to gain an understanding of the composition of the mantle source at oceanic intraplate locations, needed for a global understanding of volcanic explosivity and volatile cycles. We compare these data with complete MI studies (that include data from MI vapor bubbles) from other oceanic intraplate locations (*SI Appendix*, Table S1) that confirm that Fogo volcanics record extreme volatile contents for a nonsubduction zone volcano and that these eruptions sampled a volatile-rich source and start from a reservoir in the mantle. For comparisons, we also report olivine-hosted MI data from Tenerife in the Canary Islands (all data are included in Dataset S1, and the methods are detailed in *SI Appendix*, section 2).

2. Results and Discussion

2.1. Source Composition and Volatile Contents. After performing postentrapment crystallization (PEC) corrections (*SI Appendix*, section 7, no more than ±1.2% in the corrected volatile concentrations depending on chosen model and fO_2), all the MI compositions are basanitic in composition, consistent with the whole rock data from samples FG04, FG18, and FG19 (Fig. 2*A*). These MIs are hosted in primitive olivine phenocrysts with Mg# [molar % Mg/(Fe^{2+}+Mg)*100] of 86 to 88% for FG19 and FG18 with the most primitive close to equilibrium with the mantle (melt Mg# 70 to 71, *SI Appendix*, section 7). Sample FG04 shows more variability in olivine composition with some more primitive (Ol Mg# ~87), but the majority record a more evolved liquid (Ol Mg# 77 to 82). Trace element chemistry collected on these olivines is consistent with melts derived from melting of peridotite-dominated source for samples FG04 and FG18, and with a pyroxenitic component for FG19, both sources in the garnet stability field (ref. 44, *SI Appendix*, Figs. S13 and S14). Residual garnet is also recorded in the whole rock and MI rare-earth element concentrations (e.g., Gd/Yb > 3).

MIs at Fogo record highly oxidized mantle conditions even in the most primitive olivine (up to NiNiO +1; Fig. 2*B*) using the V-partitioning oximeter ($D_{v\ (melt/ol)}$; ref. 45) consistent with previous estimates of oxidation state at Fogo by Fe K-edge XANES (48). Silica undersaturation and extremely high CaO (up to 14 wt%) suggest derivation from a CO_2-rich source based on experimental petrology (Fig. 1*A*, ref. 27). Assuming that the most primitive MIs are representative of primary liquids, this experimental parametrization predicts an average 4.5 ± 2.7 wt% CO_2 in these melts. Considering the inherent uncertainty and the fact that other major volatiles like H_2O are not included in this model, the next logical step is to constrain these values in the MI. We identified that Fogo records extreme volatile contents (up to 2 wt% CO_2, 2.8 wt% H_2O, 6,000 ppm S, 1,900 ppm F, and 1,100 ppm Cl) in the most primitive samples (Fig. 3). These high S contents confirm the oxidizing conditions recorded by $D_{v\ (melt/ol)}$, and the overall increase in halogens and S with fractional crystallization (as Mg# in the host olivine decreases) suggests that system was closed to degassing until eruption (Fig. 3).

When compared to the available volatile data from other oceanic islands, these values represent the highest volatile contents measured thus far in primitive silica-undersaturated melts at any oceanic intraplate location on Earth (Figs. 3 and 4*A*). High volatile concentrations can often be explained due to melting style since low degrees of partial melting result in the concentration of highly incompatible elements in the melt, both volatile and involatile. However, such extreme volatile concentrations could also suggest that Fogo is sampling a volatile-rich source. Our data from Fogo highlight that Si-undersaturated melts have a higher solubility for volatile species as reported by experiments (27, 49). The fundamental question is whether these melts only represent low-degree partial melts with extremely high volatiles due to

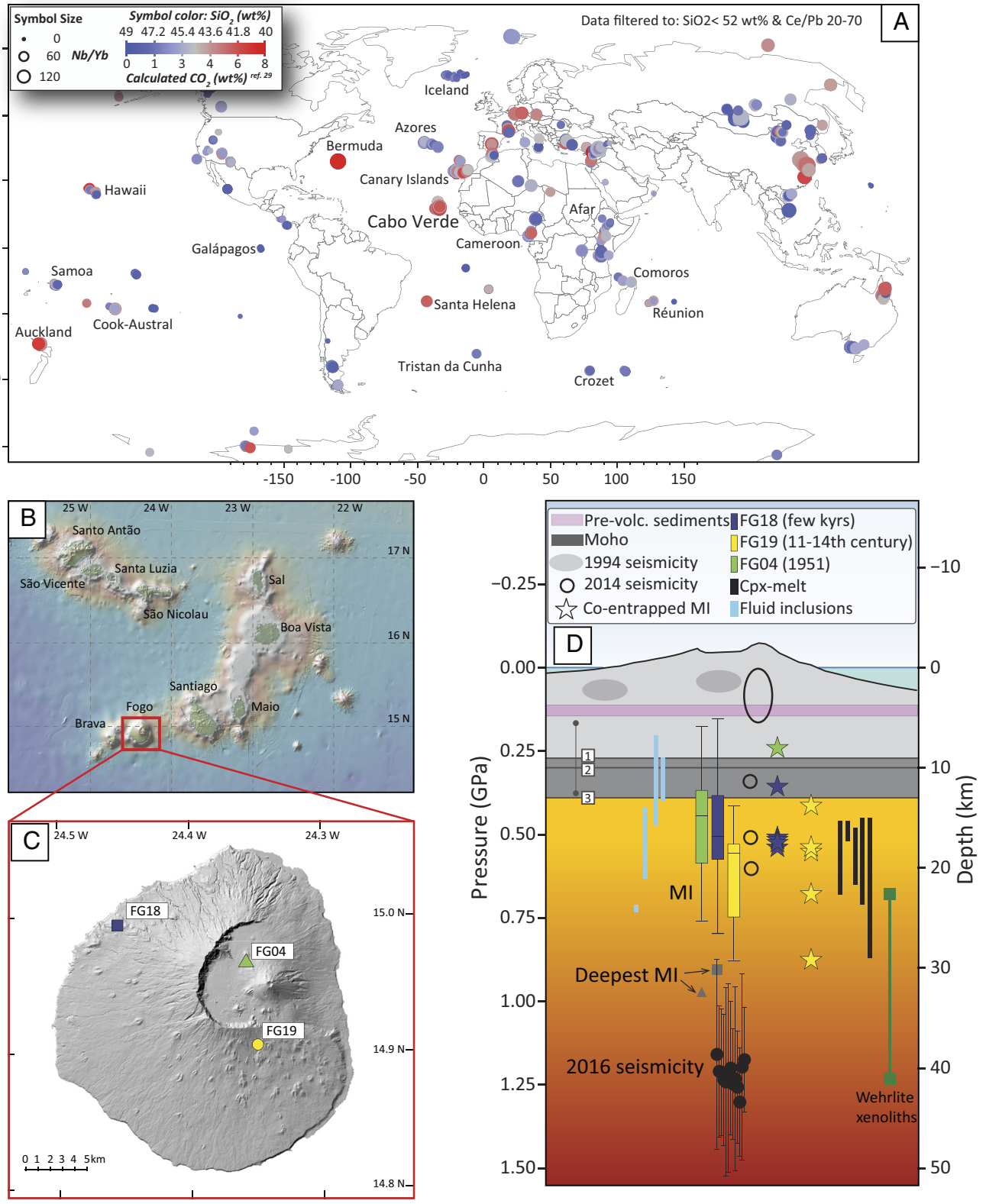

Fig. 1. Cabo Verde Islands (CVA) in the context of global intraplate volcanism. (*A*) Miocene to recent intraplate volcanoes from the GEOROC Database, highlighting Cabo Verde as a global silica-undersaturated endmember (samples filtered to SiO_2 < 52 and Ce/Pb 20 to 70): Symbol color indicates SiO_2 contents and inferred CO_2 contents of the melts at depth calculated as function of their SiO_2 contents using ref. 27, while symbol size is proportional to Nb/Yb and used as a potential mantle source enrichment indicator (28), (*B*) Map of CVA made with GeoMapApp (www.geomapapp.org)/CC BY. (*C*) Digital Elevation Model of Fogo Island, at 1:5,000 scale, with sample locations. Base model from Unidade de Coordenação do Cadastro Predial (UCCP) do Ministério do Ambiente Habitação e Ordenamento do Território (MAHOT). Cape Verde (2010), Chã das Caldeiras detail from ref. 29. (*D*) Summary figure of the plumbing system below Fogo volcano, including earthquake hypocenter depths (30–33), fluid inclusion and clinopyroxene-melt barometry (24, 30, 34, 35), wehrlite xenolith pressures from 1995 (36) shown as a dark green line with square ends, and our melt inclusion data represented in the box-and-whisker plots, with the deepest capture pressures represented in gray. The corrected cotrapped melt inclusions are included as stars, indicating the presence of an exsolved fluid up to 30 km. The prevolcanic sediment layer is shown in pink (37). The Moho depth in dark gray corresponds to 1) seismic Ps receiver functions from this study (*SI Appendix*, section 12 and Fig. S26), 2) receiver function inversions (38), and 3) controlled-source wide-angle refraction experiments (37).

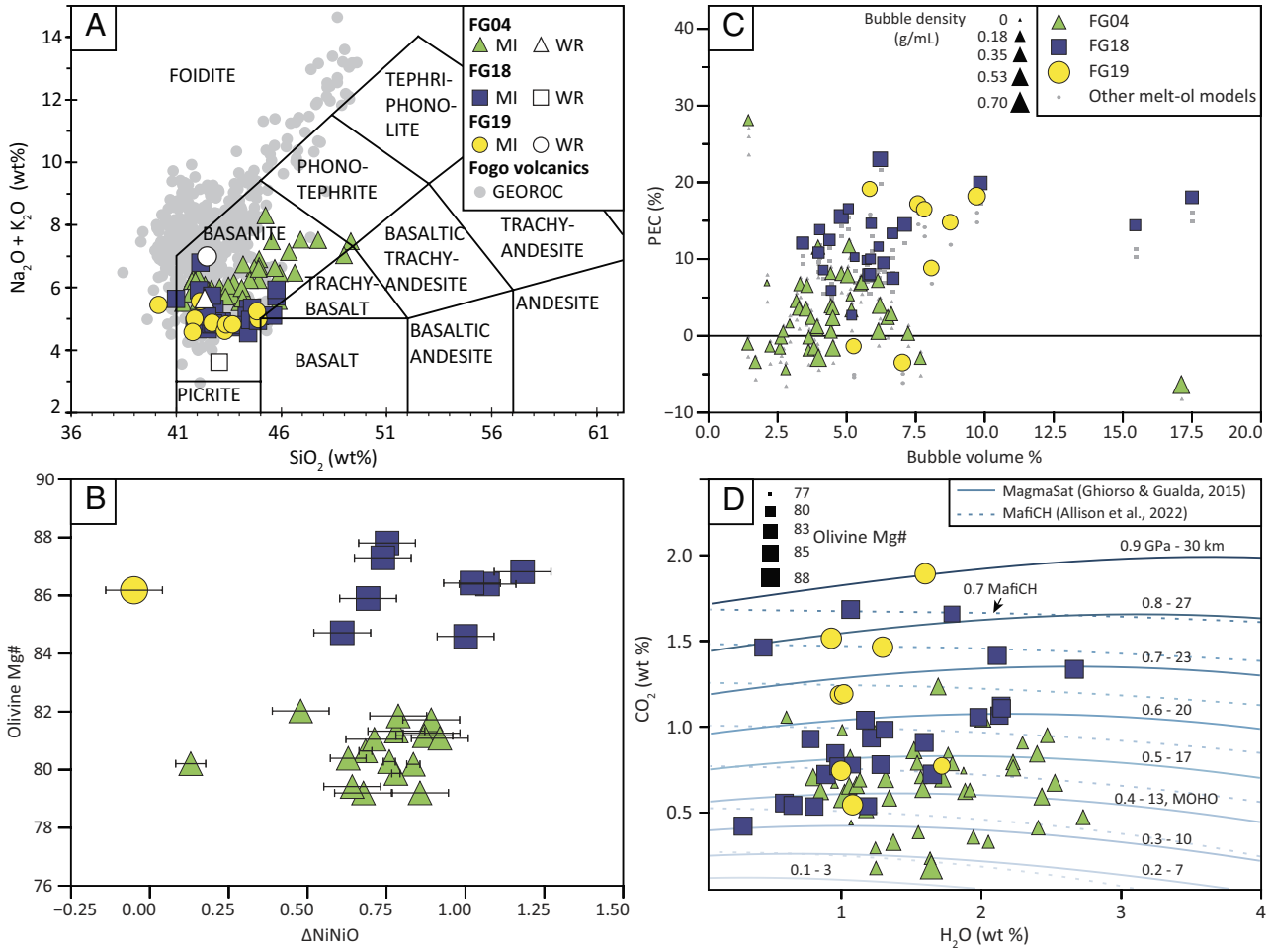

Fig. 2. Melt inclusion results from Fogo samples. (*A*) TAS diagram with PEC-corrected melt inclusion compositions compared with whole-rock data (samples FG04, FG18, and FG19) and the distribution of Fogo volcanics from the GEOROC database (gray circles). (*B*) Record of oxidation state as a function of olivine Mg#, showing the oxidizing conditions at Fogo (NiNiO 0 to +1) calculated using the V partition oximeter (45). (*C*) Vapor bubble % as a function of PEC, with symbols sized by bubble CO_2 density. The effect of different melt-olivine models on PEC corrections shown in gray is discussed in *SI Appendix*, section 7. (*D*) CO_2-H_2O variations in the Fogo melt inclusions, with symbols sized by the Mg# of the olivine host. Isobars calculated using the MagmaSat (46) and MafiCH (47) solubility models. These are corrected for PEC and heterogeneous entrapment.

volatile incompatibility during melting or whether they also sampled a source higher in volatiles. To answer this question, we plotted ratios of elements with similar partitioning behavior during melting (e.g., H_2O/Ce, S/Dy, F/Nd, and Cl/K, ref. 3 and references therein) resulting in global trends that support a source higher in volatiles for Fogo compared to the depleted MORB mantle (DMM) and Hawaii (H_2O/Ce > 250, S/Dy > 400, F/Nd > 30; Fig. 4 *B* and *C*). While higher ratios can be a result of anomalous involatile trace element depletions (50), we stress that this is not the case for our suite of Fogo MIs, which exhibit high S/Dy, F/Nd, and H_2O/Ce despite having similar or slightly higher concentrations of these elements (Ce ~60 to 125 ppm, Dy ~4 to 8 ppm, and Nd ~35 to 65 ppm) as those found at other OIBs such as Hawaii, Azores, Antarctica, and Galápagos. In particular, the S/Dy ratio for Fogo MI is significantly higher than for all other comparable OIBs at the same range of Dy content. In contrast, CO_2/Ba and CO_2/Nb are very low on account of anomalously high concentrations of Ba (~400 to 825 ppm) and Nb (50 to 100 ppm), indicating that these may not be applicable to such enriched silica-undersaturated samples (*SI Appendix*, section 8), and thus, they require further experimental petrology exploration. Interestingly, we found variability in S/Dy (~400 to 1,200), F/Nd (~20 to 50), and Cl/K (~100 to 600) ratios in Fogo MI at the same olivine-host Mg#, indicating that these MIs likely also record heterogeneity in the sampled source consistent with trace-elements record in the olivine crystals (ref. 44, *SI Appendix*, Figs. S13 and S14). This could also explain some of the differences in volatile contents that are unexplained by typical degassing pathways (Figs. 2*D* and 3). Overall, we found clear differences in the global OIB trends for halogens: Hawaii (Kīlauea and Haleakalā) exhibits DMM-like Cl/K and F/Nd, another group (Antarctica, Galápagos, and the Canary Islands) extends to high Cl/K ratios and moderate F/Nd, and finally Fogo and some Haleakalā samples extend to high F/Nd but relatively low Cl/K. The CVA and the Canary Islands are two Atlantic oceanic intraplate locations where silica-undersaturated lavas are dominant (Fig. 1*A*), and where the high S and halogens (Figs. 3 and 4), as well as H_2O-CO_2 (Fig. 2*D*), are likely recycled by deep subduction and returned by the plume, or possibly even stored in the transition zone by previous subduction events and sampled by either the plume or small-scale instabilities derived from this boundary layer (40, 41).

2.2. CO_2-Dominated Exsolved Fluid at Depths of up to ~30 km. Vapor bubbles in MI are generally formed by the growth of a denser phase (here olivine) from a less dense phase (silicate liquid) during PEC followed by shrinkage due to the differences in the coefficient of thermal expansion of the host olivine and liquid (9). That said, the complexity of a magmatic system can allow fluid

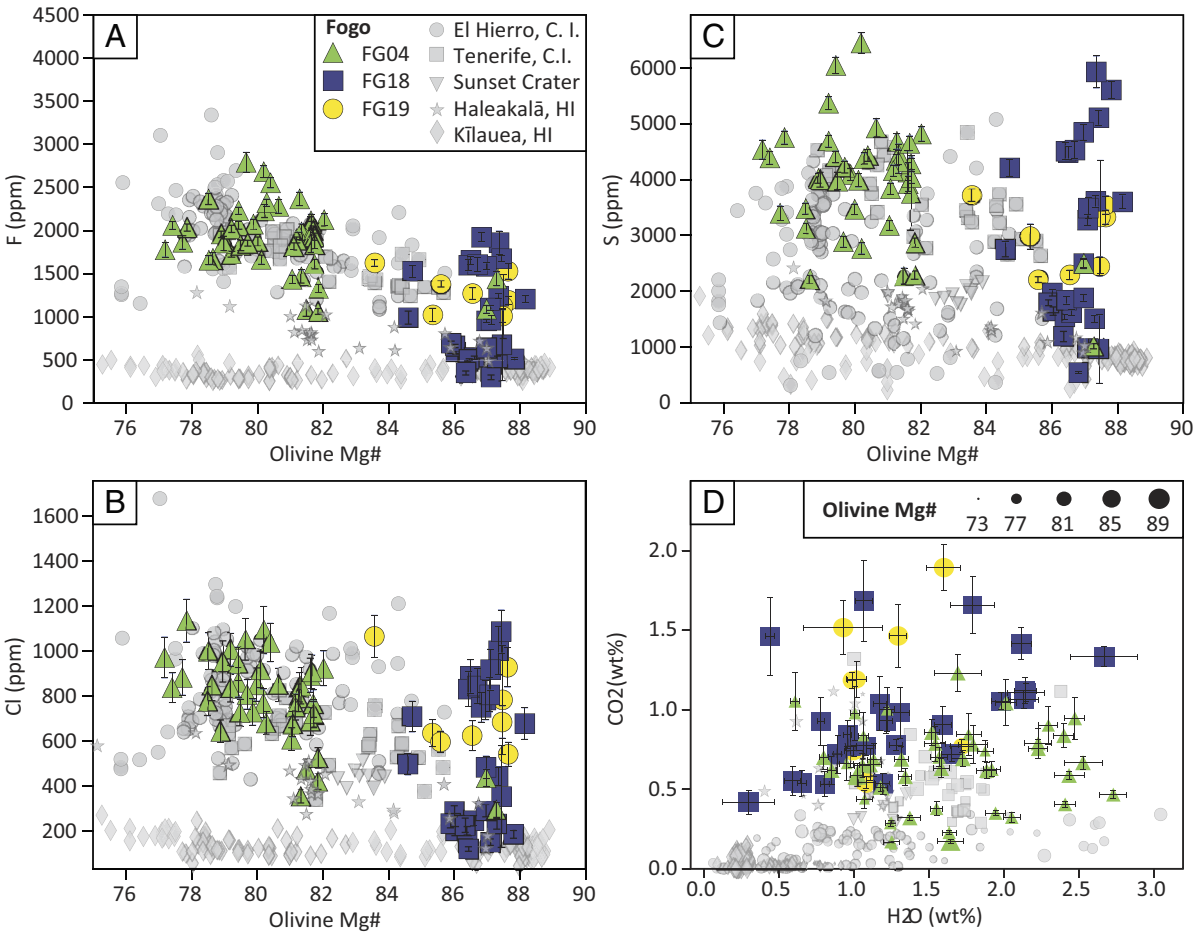

Fig. 3. Volatile contents from Fogo MIs as function of host olivine Mg# compared to MI volatile data from other alkaline intraplate volcanoes: El Hierro in gray circles (Canary Islands, Spain; references in *SI Appendix*, Table S1), Tenerife in gray squares (Canary Islands, Spain; data in this study, see *SI Appendix*), Sunset Crater in gray triangles (Arizona, USA; references in *SI Appendix*, Table S1), and Haleakalā and Kīlauea (Hawaii, USA; references in *SI Appendix*, Table S1) in gray stars and diamonds, respectively. A comprehensive list of references can be found in *SI Appendix*, Table S1. The increase of halogens and S with fractional crystallization suggests that the system was closed to degassing until eruption. Note that the Fogo samples record the highest S concentration in primitive (Mg# 86 to 88) olivine-hosted MI from oceanic intraplate volcanoes. (*A*–*B*) Halogen contents (F and Cl, respectively) as function of host olivine Mg#, (*C*) S content as function of host olivine Mg#, (*D*) CO_2 content as function of H_2O content with symbols sized according to the Mg# of the olivine host.

exsolution at depth, if the melt is volatile-saturated resulting in heterogenous entrapment of a silicate liquid and exsolved fluid phase (10). Therefore, before the volatile data were interpreted in terms of magma storage depths, we accounted for this effect. A common test for heterogeneous entrapment of MI vapor bubbles consists of comparing bubble volume to MI volume on a log:log plot (ref. 8; *SI Appendix*, Fig. S17 in *SI Appendix*, section 9). This method assumes that vapor bubbles formed by the same process should approximately follow the same isovolumetric % line. After this, a threshold of 10% in the volume % (%vol) of bubbles in MI studies is typically used as an upper limit to exclude heterogeneously entrapped vapor bubbles (8), regardless of differences inherent to the samples (i.e., melt composition, glass transition temperature, and difference between entrapment and eruptive temperature). Under these premises, all but three of our MI would be considered shrinkage bubbles, and reconstructed CO_2 contents would be artificially high (up to ~3.7 wt%). Nevertheless, it is likely that smaller %vol bubbles could have also resulted from coentrapment of fluids (10). In such cases, it may be very difficult or even impossible to discern which MIs are likely to be heterogeneously entrapped solely based on the method and threshold described above.

To better assess for heterogeneous entrapment, we modeled the two-stage growth of vapor bubbles, representative of the physical processes that MIs undergo after their capture (e.g., refs. 9, 10, and 18; *SI Appendix*, section 9). 1) A stage of high-temperature PEC-driven growth, during which melt composition and density change and a significant amount of CO_2 can diffuse into the bubble (52) and 2) a stage of rapid syn-eruptive cooling growth, driven by the thermal contraction of the melt as it cools to the glass transition temperature and during which the bubble may grow to much larger extent. If PEC and syn-eruptive growth are the only two processes that MI undergo, bubbles with larger %vol should have lower CO_2 densities than bubbles with lower %vol in MI that experienced the same amount of PEC. In Fogo MI, bubbles with more PEC often show higher CO_2 densities (Fig. 2*C*); however, larger %vol bubbles often record higher densities (up to 0.7 g/mL) than lower bubble %vol bubbles with the same amount of PEC, inconsistent with solely postentrapment bubble growth. Additionally, the bubble growth model predicts a maximum volume of ~6 ± 1.5 vol% for Fogo MI (considering transition temperature and volume uncertainties). We note that in Fogo MI, the bubbles that occupy more than the maximum modeled bubble %vol for each MI also show higher CO_2 densities at similar amounts of PEC (Fig. 2*C*). We therefore conclude that ~10% of Fogo MI were heterogeneously entrapped as melt and exsolved fluid.

To correct the CO_2 contents of heterogeneously entrapped MI, we ran simulations of CO_2 loss to basanitic MI vapor bubbles containing 0 to 10 vol% cotrapped fluid, undergoing 0 to 20% PEC,

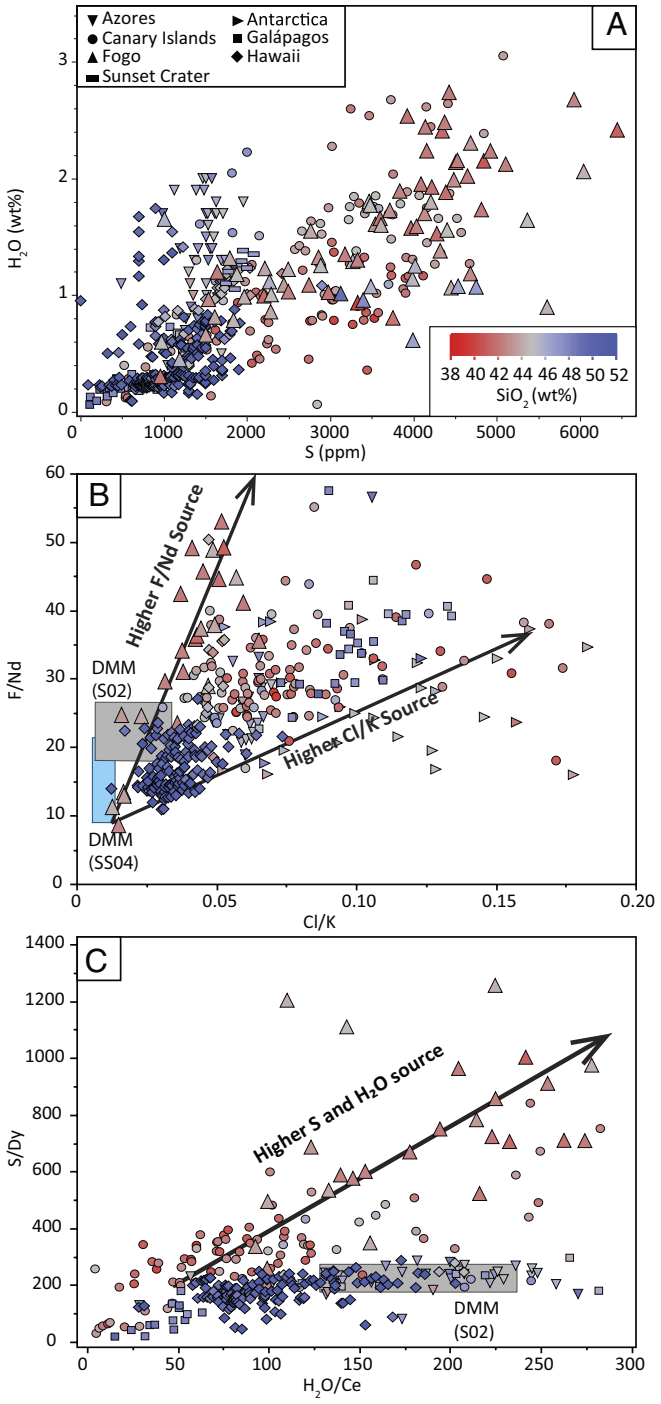

Fig. 4. Source volatiles recorded in Fogo MI compared to MI data from other intraplate volcanoes including Pico, in Azores; El Hierro, and Tenerife in the Canary Islands; Floreana in the Galápagos; Kīlauea, Mauna Loa, Lō'ihi (Kama'ehuakanaloa), and Haleakalā in Hawaii; McMurdo in the Ross Sea Rift in Antarctica; and Sunset Crater in Arizona (*SI Appendix*, Table S1). (*A*) H_2O as a function of S, with symbols colored SiO_2 content (correlates with CO_2 content, see Fig. 1*A*). (*B*) F/Nd ratio as a function of Cl/K ratio with symbols colored by SiO_2 content. Depleted MORB Mantle (DMM) sources are taken from ref. 3 ("S02") and ref. 51 ("SS04"). (*C*) S/Dy ratio as a function of H_2O/Ce ratio colored by SiO_2 content. Note that Fogo shows little to no degassing compared to DMM as indicated by the H_2O/Ce ratios and displays a strong enrichment in S, indicating an S-rich source (S/Dy). The only other location for which data were available that displays relative S enrichment is El Hierro (Canary Islands).

and starting at 500 and 700 MPa with the model of refs. 52 and 53. Using the amount of PEC for each MI, the estimated cotrapped bubble %vol from our bubble growth model, and average saturation pressure for each eruption, we recalculated the original dissolved CO_2 contents and saturation pressures for MI with cotrapped bubbles (*SI Appendix*, sections 9 and 10). Saturation pressures for MI at Fogo indicate that they were trapped at variable depths from relatively shallow in the crust (~10 km) to mantle pressures up to ~600 to 900 MPa or ~20 to 30 km using a pressure gradient of ~30 MPa/km (Fig. 2*D*). We note that CO_2 is the predominant exsolved volatile component in our MI (>90 mol%). Additionally, corrected pressures for MI that were heterogeneously entrapped indicate that nearly pure CO_2 exsolved fluids were present in the plumbing system at Fogo at depths of up to ~30 km, which is consistent with recent findings of near-pure CO_2 fluid inclusions captured at up to ~24 km at Fogo (34). Trapping of Fogo MI at mantle depths of up to 20 to 30 km is also consistent with the presence of wehrlite xenoliths that record pressures of 22 to 42 km carried by other Fogo eruptions (36) as well as the estimated depth of the 1995 magma reservoir at >16.5 km based on an InSAR deformation model (54).

2.3. Plumbing System and Volatile Evolution at Fogo. Our MI entrapment pressures are broadly consistent with estimates from clinopyroxene-melt barometry (Fig. 1*D*) and CO_2-rich fluid inclusions (23, 24, 30, 34, 35) and indicate melt migration from mantle pressures around 20 to 30 km (where the most mafic record the highest pressures) to magma temporarily stalling at ~15 to 18 km), where the majority of MIs were entrapped. Our data are also consistent with a transient shallower magma reservoir at the Moho (~10 to 13 km) represented by MI hosted in the most fractionated olivine (sample FG04, Mg# 77 to 82) and that has been reported previously (24, 30, 34, 35, 55). While we recognize that the uncertainty in melt inclusion saturation pressures is fairly large, especially given bubble volume and solubility model uncertainties, these depths of entrapment are consistent with previously reported storage regions identified by the presence of near-pure CO_2-rich fluid inclusions for which relatively small uncertainties reliably permit the identification of several storage regions (24, 30, 34, 35, 56). Our findings also indicate the presence of exsolved fluids, rich in CO_2 (>90 mol%, calculated fluid composition in equilibrium with the MI), at pressures of up to ~900 MPa, indicating an already bubbly magma at ~30 km depth. At Fogo, earthquakes have been identified at mantle depths (~30 to 40 km, ref. 31, and at shallower depths <10 km, while our MIs seem to be ubiquitously trapped at depths in between, suggesting that most of the melt storage is between those hypocenter locations. Deep magma storage has been identified as a common feature of ocean islands (55), although most of this evidence comes from clinopyroxene-melt barometry, seismicity, and sparse fluid inclusion data (mainly in the Azores and Cabo Verde). In many locations, shallow magma storage also appears to be common. However, this is not the case at Fogo where evidence is lacking for anything other than transient syn-eruptive shallow storage and geophysical evidence rather points to melting well below 10 km (57) and eruptions being fed directly from sub-Moho storage as was the case of the 2014 to 2015 eruption (30, 55, 58). Our MI data appear to be direct geochemical evidence of this as well.

We estimated decompression rates for these eruptions using the method of ref. 59 based on MI sizes, location, and H_2O loss. Our results indicate that these magmas ascended with decompression rates of ~0.005 to 0.05 MPa/s for FG18 and FG19 and 0.005 to 0.0005 MPa/s for FG04 (*SI Appendix*, section 11), consistent with explosive eruptions of relatively low intensity (Volcanic Explosivity Index – VEI 2-3) like the 1992 eruption of Cerro Negro (11), the 1977 eruption of Seguam or Kīlauea Iki (59). These decompression rates correspond to 2 to 22 h from Moho depth (~13 km from ref. 37; 9.05 ± 3.80 km at Fogo via receiver functions in this study;

SI Appendix, section 12 and Fig. S26) for FG18 and FG19 assuming a constant decompression rate for the entire ascent and 1 to 9 d for FG04. This suggests that the prehistoric eruptions represented by samples FG18 and FG19 were more explosive than the eruption of 1951, which is consistent with their larger cinder cones. Although we recognize that this approach assumes that H_2O starts to degas significantly at these depths, we note that these estimates agree with the record of re-equilibration of fluid inclusions from Fogo that indicated stagnation at Moho depths in the order of hours to days prior to recent eruptions (24, 35) and with the zonation of olivine in the 2014 to 2015 eruption that recorded stagnation for no more than a day and ascent from the Moho in <12 h (30).

While H_2O exsolution is often invoked as the main driver of decompression and ascent in explosive eruptions due to the late degassing behavior compared to CO_2 (18), a role for CO_2 in the ascent and explosivity of some mafic eruptions such as the sub-Plinian eruption of Sunset Crater (continental intraplate), as well as Cerro Negro (subduction volcano), has previously been proposed (10, 11). Additionally, explosive eruptions at Kīlauea were statistically linked to higher volatile concentrations in primary melts (22) and suggested to bypass the shallow storage being fed directly from a deeper source. The high saturation pressure and CO_2 contents indicated by our MI data show that CO_2 clearly plays a major role at Fogo volcano. Specifically, at these high pressures, solubility models indicate that CO_2 is the dominant volatile component (90% mol) in the exsolved fluid at Fogo volcano. Geophysical evidence also indicates that eruptions are fed by vertical propagation of dikes from sub-Moho depths to the surface, with a lack of evidence for shallow magma reservoirs (where H_2O would begin to dominate in the fluid phase) (55, 57, 58). Finally, magma ascent assisted by exsolved CO_2 is expected to be a self-accelerating process by buoyancy decrease. A likely scenario starts with CO_2 exsolution initiating dike fracture by overpressure, and as the melt continues to ascend, the density of the exsolved CO_2 decreases, enhancing buoyancy and driving an accelerated ascent of the magma which in turn facilitates further degassing. Therefore, CO_2 exsolution must play a critical role in driving the ascent of mafic explosive eruptions that evolve at mantle depths in volcanoes that sample volatile-rich sources, making the eruption style in such cases an inherited characteristic from the mantle source.

3. Materials and Methods Summary

We selected olivine crystals coated in glass from the fine tephra of three samples from two prehistoric and one historic (1951) eruptions of Fogo, from these materials we selected primary MI with no obvious evidence of strong decrepitation or H_2O loss. We measured the MI and bubble volumes by a combination of calibrated optical methods and nano-X-ray computed tomography data. Raman spectra were acquired using two WiTec Alpha 300R Raman spectrometers fully calibrated for CO_2 Raman Spectroscopy at the Department of Earth and Atmospheric Sciences at Cornell University (Gazel's lab) and Cornell Center for Materials Research (CCMR). We conducted 1 atm heating experiments in a LINKAM TS1400XY for MI that contained significant carbonate on the walls of the vapor bubbles to resorb the carbonate with as little impact on the MI composition as possible. All MIs were glassy after quenching. We remeasured the bubble CO_2 densities after heating experiments and compared the results in *SI Appendix*, section 5 and Fig. S12. Overall, only MIs with significant or large amounts of carbonate detected via Raman prior to heating showed a significant increase in total CO_2 after heating. After Raman analysis and heating experiments, MIs were polished to expose the glass and pressed in Indium and gold-coated for Secondary Ion Mass Spectrometry (SIMS) analysis. SIMS analysis was conducted at Woods Hole Oceanographic Institution using a CAMECA IMS 1280 Secondary Ion Mass spectrometer and a Cs^+ microbeam to obtain CO_2, H_2O, S, Cl, and F measurements on the MI glasses. Whole-rock major elements were analyzed at the GeoAnalytical Lab at Washington State University. MI glasses were analyzed for major elements using a Cameca SX5 electron microprobe at Syracuse University, NY. Trace elements were analyzed in MI glasses and olivines using an Agilent 8900 Triple Quad Mass Spec equipped with a Coherent COMPex 102 F 193 nm high-powered excimer laser at the CMaS facilities at Cornell University.

We corrected the MI compositions for the effect of postentrapment crystallization (PEC) and Fe loss via the software Petrolog3 (60) using Fe total from whole-rock data for each sample (further details in *SI Appendix*, section 7). These corrections were calculated using an oxidation state equal to the NNO+1 buffer based on our trace element data, which is also consistent with recent estimates of fO_2 for Fogo (48). To assess for heterogeneous entrapment of our MI vapor bubbles, we modeled the growth of a vapor bubble in an MI upon cooling through the method described in refs. 9 and 10. We consider that vapor bubbles with a %vol more than 1.5 units above the maximum modeled %vol to be heterogeneously entrapped. We then use simulations of CO_2 loss to heterogeneously entrapped vapor bubbles at high pressure (500 to 700 MPa) for basanitic compositions (53) to restore the CO_2 contents of vapor bubbles that contained a preexisting CO_2-rich fluid. We calculate MI saturation pressures using MagmaSat (46) and MafiCH (47) solubility models. We refer the reader to the *SI Appendix* for exhaustive details on our methodology.

Data, Materials, and Software Availability. All data are available in the supplement (Dataset S1). The bubble growth model is available as a Python3 Jupyter Lab notebook (Dataset S2) along with the necessary input file (Dataset S3) in the supplement. We note that the data contained in the input file (Dataset S3) for the Jupyter Lab notebook (Dataset S2) is also available under tab "Bubble Growth Model" in Dataset S1, but it has been formatted to run with the notebook as is in Dataset S3.

ACKNOWLEDGMENTS. We are grateful to an anonymous reviewer and J. Maclennan whose comments and suggestions helped improve the original manuscript. We appreciate the editorial work of PNAS. NSF EAR award Nos. 1826673 and 1802012 (E.G.). Fundação para a Ciência e a Tecnologia I.P. (FCT): IF/01641/2015 MEGAWAVE (R.S.R.). FCT and European Regional Development Fund through Programa Operacional Regional de Lisboa (POR Lisboa 2020): project PTDC/CTA-GEO/28588/2017 – LISBOA-01-0145-FEDER-028588 UNTIeD. (R.S.R.). NIH: Imaging data were acquired through the Cornell Institute of Biotechnology's Imaging Facility, with NIH 1S10OD012287 funding for the Zeiss-Xradia Versa 520 X-ray microscope. Biotechnology Resource Center at Cornell University: SEED grant (E.G. and C.L.D.)

Author affiliations: [a]Department of Earth and Atmospheric Sciences, Cornell University, Ithaca, NY 14850; [b]School of Earth and Environmental Sciences, Cardiff University, Cardiff CF10 3AT, United Kingdom; [c]Instituto Dom Luiz and Departamento de Geologia, Faculdade de Ciências, Universidade de Lisboa, 1749-016 Lisbon, Portugal; [d]Lamont-Doherty Earth Observatory, Climate School, Columbia University, Palisades, NY 10964-8000; [e]Lunar and Planetary Institute, Universities Space Research Association, Houston, TX 77058; [f]Astromaterials Research and Exploration Sciences, NASA Johnson Space Center, Houston, TX 77058; [g]Department of Earth and Atmospheric Sciences, University of Alberta, Edmonton, AB T6G 2R3, Canada; [h]Jackson School of Geosciences, The University of Texas at Austin, Austin, TX 78712; [i]Department of Geosciences, Baylor University, Waco, TX 76706; [j]Department of Geosciences, Virginia Tech, Blacksburg, VA 24061; [k]Geología de terrenos volcánicos, Universidad de Las Palmas de Gran Canaria, Las Palmas 35001, España; and [l]Woods Hole Oceanographic Institution, MA 02543

Author contributions: C.L.D. and E.G. conceptualized the study, designed research and wrote the main paper; C.L.D., S.V., J.H., C.M.A., L.R.M., and B.M. performed research; C.L.D., R.S.R., M.S.-M., and J.C.C. contributed new reagents/analytic tools; C.L.D., C.M.A., L.R.M., and B.M. analyzed data; C.L.D. conceptualization, experimental design, sample preparation, data acquisition, data processing and analyses, original full draft manuscript writing (including supplementary materials), review, and figure preparation. Python bubble growth model writing and implementation; E.G. conceptualization, experimental design, main text manuscript writing, manuscript review, Fig. 1*A* preparation, and funding PI; R.S.R. field sample collection, Fig. 1*C* panel preparation, and manuscript review; S.V. sample preparation assistance and processing, data compilation assistance, and manuscript review; M.S.-M. thermodynamic modelling and manuscript review; J.H. receiver function analysis and manuscript review; C.M.A. tenerife melt inclusion data acquisition and manuscript review; L.R.M. tenerife melt inclusion sample preparation and analysis and manuscript review; J.C.C. tenerife sample field collection and manuscript review; B.M. SIMS data acquisition and manuscript review and edition.

1. R. Dasgupta, M. M. Hirschmann, The deep carbon cycle and melting in Earth's interior. *Earth Planet. Sci. Lett.* **298**, 1 (2010).
2. G. A. Gaetani, T. L. Grove, The influence of water on melting of mantle peridotite. *Contrib. Mineral. Petrol.* **131**, 323–346 (1998).
3. A. E. Saal, E. H. Hauri, C. H. Langmuir, M. R. Perfit, Vapour undersaturation in primitive mid-ocean-ridge basalt and the volatile content of Earth's upper mantle. *Nature* **419**, 451–455 (2002).
4. J. A. Crisp, Rates of magma emplacement and volcanic output. *J. Volcanol. Geotherm. Res.* **20**, 177–211 (1984).
5. Z. Taracsák *et al.*, High fluxes of deep volatiles from ocean island volcanoes: Insights from El Hierro, Canary Islands. *Geochim. Cosmochim. Acta* **258**, 19–36 (2019).
6. P. E. Wieser *et al.*, Reconstructing magma storage depths for the 2018 Kīlauean eruption from melt inclusion co2 contents: The importance of vapor bubbles. *Geochem. Geophys. Geosyst.* **22**, e2020GC009364 (2021).
7. M. E. Hartley, J. Maclennan, M. Edmonds, T. Thordarson, Reconstructing the deep CO2 degassing behaviour of large basaltic fissure eruptions. *Earth Planet. Sci. Lett.* **393**, 120–131 (2014).
8. L. R. Moore *et al.*, Bubbles matter: An assessment of the contribution of vapor bubbles to melt inclusion volatile budgets. *Am. Mineral.* **100**, 806–823 (2015).
9. E. M. Aster *et al.*, Reconstructing CO2 concentrations in basaltic melt inclusions using Raman analysis of vapor bubbles. *J. Volcanol. Geotherm. Res.* **323**, 148–162 (2016).
10. C. M. Allison, K. Roggensack, A. B. Clarke, Highly explosive basaltic eruptions driven by CO 2 exsolution. *Nat. Commun.* **12**, 1–10 (2021).
11. K. Roggensack, R. L. Hervig, S. B. McKnight, S. N. Williams, Explosive basaltic volcanism from Cerro Negro Volcano: Influence of volatiles on eruptive style. *Science* **277**, 1639–1642 (1997).
12. M. Cassidy, M. Manga, K. Cashman, O. Bachmann, Controls on explosive-effusive volcanic eruption styles. *Nat. Commun.* **9**, 2839 (2018).
13. H. M. Gonnermann, M. Manga, The fluid mechanics inside a volcano. *Annu. Rev. Fluid Mech.* **39**, 321–356 (2007).
14. A. Costa, O. Melnik, E. Vedeneeva, Thermal effects during magma ascent in conduits. *J. Geophys. Res. Solid Earth* **112** (2007).
15. W. Degruyter, C. Huber, O. Bachmann, K. M. Cooper, A. J. R. Kent, Magma reservoir response to transient recharge events: The case of Santorini volcano (Greece). *Geology* **44**, 23–26 (2016).
16. E. C. Bamber *et al.*, Pre- and syn-eruptive conditions of a basaltic Plinian eruption at Masaya Volcano, Nicaragua: The Masaya Triple Layer (2.1 ka). *J. Volcanol. Geotherm. Res.* **392**, 106761 (2020).
17. T. Shea, J. E. Hammer, Kinetics of cooling- and decompression-induced crystallization in hydrous mafic-intermediate magmas. *J. Volcanol. Geotherm. Res.* **260**, 127–145 (2013).
18. J. Maclennan, Bubble formation and decrepitation control the CO2 content of olivine-hosted melt inclusions. *Geochem. Geophys. Geosyst.* **18**, 597–616 (2017).
19. F. Arzilli *et al.*, Magma fragmentation in highly explosive basaltic eruptions induced by rapid crystallization. *Nat. Geosci.* **12**, 1023–1028 (2019).
20. M. Edmonds *et al.*, Chapter 16 Pre-eruptive vapour and its role in controlling eruption style and longevity at Soufrière Hills Volcano. *Geol. Soc. Lond. Mem.* **39**, 291–315 (2014).
21. I. Sides *et al.*, Magma mixing and high fountaining during the 1959 Kīlauea Iki eruption, Hawai 'i. *Earth Planet. Sci. Lett.* **400**, 102–112 (2014).
22. I. R. Sides, M. Edmonds, J. Maclennan, D. A. Swanson, B. F. Houghton, Eruption style at Kīlauea Volcano in Hawai'i linked to primary melt composition. *Nat. Geosci.* **7**, 464–469 (2014).
23. J. Mata *et al.*, The 2014–15 eruption and the short-term geochemical evolution of the Fogo volcano (Cape Verde): Evidence for small-scale mantle heterogeneity. *Lithos* **288–289**, 91–107 (2017).
24. E. Hildner, A. Klügel, F. Hauff, Magma storage and ascent during the 1995 eruption of Fogo, Cape Verde Archipelago. *Contrib. Mineral. Petrol.* **162**, 751 (2011).
25. J. M. Castro, Y. Feisel, Eruption of ultralow-viscosity basanite magma at Cumbre Vieja, La Palma, Canary Islands. *Nat. Commun.* **13**, 3174 (2022).
26. S. Eisele *et al.*, Pleistocene to Holocene offshore tephrostratigraphy of highly explosive eruptions from the southwestern Cape Verde Archipelago. *Mar. Geol.* **369**, 233–250 (2015).
27. C. Sun, R. Dasgupta, Thermobarometry of CO2-rich, silica-undersaturated melts constrains cratonic lithosphere thinning through time in areas of kimberlitic magmatism. *Earth Planet. Sci. Lett.* **550**, 116549 (2020).
28. J. A. Pearce, Geochemical fingerprinting of oceanic basalts with applications to ophiolite classification and the search for Archean oceanic crust. *Lithos* **100**, 14–48 (2008).
29. G. Vieira, C. Mora, P. Pina, R. Ramalho, R. Fernandes, UAV-based very high resolution point cloud, digital surface model and orthomosaic of the Chã das Caldeiras lava fields (Fogo, Cabo Verde). *Earth Syst. Sci. Data* **13**, 3179–3201 (2021).
30. A. Klügel, S. Day, M. Schmid, B. Faria, Magma plumbing during the 2014–2015 eruption of Fogo (Cape Verde Islands). *Front. Earth Sci.* **8** (2020).
31. C. Leva, G. Rümpker, F. Link, I. Wölbern, Mantle earthquakes beneath Fogo volcano, Cape Verde: Evidence for subcrustal fracturing induced by magmatic injection. *J. Volcanol. Geotherm. Res.* **386**, 106672 (2019).
32. H. Silva *et al.*, Seismic activity in Fogo and Brava Islands, Cape Verde. *L'éruption Volcanique 1995 Sur L'î Fogo Cap-Vert*, 79–91 (1997).
33. S. I. N. Heleno, J. Fonseca, A seismological investigation of the Fogo Volcano, Cape Verde Islands: Preliminary results. *Volcanol. Seism.* **20**, 199–217 (1999).
34. F. M. L. Forte, A. Aiuppa, S. G. Rotolo, V. Zanon, Temporal evolution of the Fogo Volcano magma storage system (Cape Verde Archipelago): A fluid inclusions perspective. *J. Volcanol. Geotherm. Res.* **433**, 107730 (2023).
35. E. Hildner, A. Klügel, T. H. Hansteen, Barometry of lavas from the 1951 eruption of Fogo, Cape Verde Islands: Implications for historic and prehistoric magma plumbing systems. *J. Volcanol. Geotherm. Res.* **217–218**, 73–90 (2012).
36. J. M. Munha, M. H. Mendes, T. Palácios, L. C. Silva, P. C. Torres, Petrologia e geoquimica da erupcao de 1995 e de outras lavas historicas na ilha do Fogo, Cabo Verde. *Erupcao Vulcanica De* 171–176 (1995).
37. J. Pim, C. Peirce, A. B. Watts, I. Grevemeyer, A. Krabbenhoeft, Crustal structure and origin of the Cape Verde Rise. *Earth Planet. Sci. Lett.* **272**, 422–428 (2008).
38. L. Vinnik *et al.*, Cape Verde hotspot from the upper crust to the top of the lower mantle. *Earth Planet. Sci. Lett.* **319–320**, 259–268 (2012).
39. R. A. S. Ramalho, *Building the Cape Verde Islands* (Springer Science & Business Media, 2011).
40. S. E. Mazza *et al.*, Sampling the volatile-rich transition zone beneath Bermuda. *Nature* **569**, 398–403 (2019).
41. G. Zeng *et al.*, Nephelinites in eastern China originating from the mantle transition zone. *Chem. Geol.* **576**, 120276 (2021).
42. S. W. French, B. Romanowicz, Broad plumes rooted at the base of the Earth's mantle beneath major hotspots. *Nature* **525**, 95–99 (2015).
43. A. Aiuppa *et al.*, The fumarolic CO2 output from Pico do Fogo Volcano (Cape Verde). *Ital. J. Geosci.* **139**, 325–340 (2020).
44. A. V. Sobolev *et al.*, The amount of recycled crust in sources of mantle-derived melts. *Science* **316**, 412–417 (2007).
45. D. Canil, Vanadium in peridotites, mantle redox and tectonic environments: Archean to present. *Earth Planet. Sci. Lett.* **195**, 75–90 (2002).
46. M. S. Ghiorso, G. A. R. Gualda, An H2O–CO2 mixed fluid saturation model compatible with rhyolite-MELTS. *Contrib. Mineral. Petrol.* **169**, 53 (2015).
47. C. M. Allison, K. Roggensack, A. B. Clarke, MafiCH: A general model for H2O–CO2 solubility in mafic magmas. *Contrib. Mineral. Petrol.* **177**, 40 (2022).
48. Y. Moussallam *et al.*, Mantle plumes are oxidised. *Earth Planet. Sci. Lett.* **527**, 115798 (2019).
49. C. M. Allison, K. Roggensack, A. B. Clarke, H2O–CO2 solubility in alkali-rich mafic magmas: New experiments at mid-crustal pressures. *Contrib. Mineral. Petrol.* **174**, 58 (2019).
50. W. G. R. Miller *et al.*, Estimating the carbon content of the deep mantle with Icelandic melt inclusions. *Earth Planet. Sci. Lett.* **523**, 115699 (2019).
51. V. J. M. Salters, A. Stracke, Composition of the depleted mantle. *Geochem. Geophys. Geosyst.* **5** (2004).
52. M. Steele-Macinnis, R. Esposito, R. J. Bodnar, Thermodynamic model for the effect of post-entrapment crystallization on the H2O–CO2 systematics of vapor-saturated, silicate melt inclusions. *J. Petrol.* **52**, 2461–2482 (2011).
53. M. Steele-MacInnis, R. Esposito, L. R. Moore, M. E. Hartley, Heterogeneously entrapped, vapor-rich melt inclusions record pre-eruptive magmatic volatile contents. *Contrib. Mineral. Petrol.* **172**, 18 (2017).
54. F. Amelung, S. Day, InSAR observations of the 1995 Fogo, Cape Verde, eruption: Implications for the effects of collapse events upon island volcanoes. *Geophys. Res. Lett.* **29**, 47-1-47–4 (2002).
55. A. K. Barker, E. M. Rydeblad, S. M. D. M. Silva "Magma storage at ocean islands: Insights from Cape Verde" in *Geophysical Monograph Series*, Masotta M., Beier C., Mollo S., Eds. (Wiley, ed. 1, 2021), pp. 45–78.
56. K. Dayton *et al.*, Deep magma storage during the 2021 La Palma eruption. *Sci. Adv.* **9**, eade7641 (2023).
57. J. Carvalho, G. Silveira, S. Dumont, R. Ramalho, 3D-ambient noise surface wave tomography of Fogo volcano, Cape Verde. *J. Volcanol. Geotherm. Res.* **432**, 107702 (2022).
58. P. J. González *et al.*, The 2014–2015 eruption of Fogo volcano: Geodetic modeling of Sentinel-1 TOPS interferometry. *Geophys. Res. Lett.* **42**, 9239–9246 (2015).
59. A. Barth *et al.*, Magma decompression rate correlates with explosivity at basaltic volcanoes – Constraints from water diffusion in olivine. *J. Volcanol. Geotherm. Res.* **387**, 106664 (2019).
60. L. V. Danyushevsky, P. Plechov, Petrolog 3: Integrated software for modeling crystallization processes. *Geochem. Geophys. Geosystems* **12** (2011).